







Cite this: *Nanoscale*, 2020, **12**, 16596

# Using HAADF-STEM for atomic-scale evaluation of incorporation of antibacterial Ag atoms in a $\beta$ -tricalcium phosphate structure†

Ozkan Gokcekaya,  <sup>a</sup> Kyosuke Ueda,  <sup>b</sup> Takayuki Narushima  <sup>b</sup> and Takayoshi Nakano  <sup>a</sup>

Structural evaluation of ionic additions in calcium phosphates that enhance their performance is a long-lasting area of research in the field of biomedical materials. Ionic incorporation in  $\beta$ -tricalcium phosphate ( $\beta$ -TCP) structures is indispensable for obtaining desirable properties for specific functions and applications. Owing to its complex structure and beam-sensitive nature, determining the extent of ion incorporation and its corresponding location in the  $\beta$ -TCP structure is challenging. Further, very few experimental studies have been able to estimate the location of Ag atoms incorporated in a  $\beta$ -TCP structure while considering the associated changes in lattice parameters. Although the incorporation alters the lattice parameters, the alteration is not significant enough for estimating the location of the incorporated Ag atoms. Here, Ag incorporation in a  $\beta$ -TCP structure was evaluated on atomic scale using scanning transmission electron microscopy (STEM). To the best of our knowledge, this is the first report to unambiguously determine the location of the incorporated Ag atoms in the  $\beta$ -TCP structure by comparing  $z$ -contrast profiles of the Ag and Ca atoms by combining the state-of-art STEM observations and STEM image simulations. The Ag incorporation in the Ca(4) sites of  $\beta$ -TCP, as estimated by the Rietveld refinement, was in good agreement with the high-angle annular dark-field STEM observations and the simulations of the location of Ag atoms for [001] and [010] zone axes.

Received 2nd June 2020,  
Accepted 28th July 2020  
DOI: 10.1039/d0nr04208k  
[rsc.li/nanoscale](http://rsc.li/nanoscale)

## 1. Introduction

Calcium phosphates (CaPs) have long received a great deal of attention as a primary group of candidates for many biomedical applications such as resorbable and non-resorbable ceramics, cements, drug carriers, prosthetic coatings, and composite materials for bone reconstruction and replacement, bone defect-filling, drug carrier, and coatings of metal prostheses.<sup>1,2</sup> The incorporation of various atoms in both cation and anion sites has been studied to improve the structural, physical, and chemical properties of CaPs to sustain thermal stability, control dissolution, obtain antibacterial property, and improve osteoblast differentiation and osteoclast

proliferation.<sup>3–7</sup> Among these CaPs, particular attention has been given to  $\beta$ -tricalcium phosphate ( $\text{Ca}_3(\text{PO}_4)_2$ ,  $\beta$ -TCP) owing to its resorbability *in vivo* accompanied by new bone growth and replacement.<sup>8,9</sup>

$\beta$ -TCP has a rhombohedral structure with a space group of  $R3c$ , described by A and B columns running along the  $c$ -axis (ESI Fig. S1†).<sup>10</sup> The structure of  $\beta$ -TCP allows ionic replacements, especially the incorporation of cations at the calcium sites in the A columns.<sup>11–13</sup> Calcium ions in  $\beta$ -TCP are present in five locations. Ca(1), Ca(2), and Ca(3) sites are at stable positions with eight coordinated oxygen atoms on a densely packed B column. The A column of  $\beta$ -TCP has the form of  $\text{PO}_4\text{--Ca(4)--Ca(5)--}$ , where Ca(4) and Ca(5) sites are at special positions with a multiplicity of 1/3 of the other Ca sites, allowing easy incorporation of various ions.<sup>14,15</sup>

Ag incorporation in CaPs has been investigated to achieve antibacterial activity by the release of Ag atoms in the human body.<sup>16–24</sup> However, to date, due to the limitations of analytical techniques, very few experimental studies have provided quantitative information on capacity of Ag incorporation into the  $\beta$ -TCP structure.<sup>25</sup> It is essential to elucidate the limit of incorporation of Ag atoms in the  $\beta$ -TCP structure with respect to the incorporation sites. To understand the mechanism of the

<sup>a</sup>Division of Materials and Manufacturing Science, Graduate School of Engineering, Osaka University, 2-1 Yamadaoka, Suita, Osaka, 565-0871, Japan

<sup>b</sup>Department of Materials Processing, Tohoku University, 6-6-02 Aza Aoba, Aramaki, Aoba-ku, Sendai, Miyagi 980-8579, Japan

†Electronic supplementary information (ESI) available: Notation and composition of specimens. Details of TEM-EDS line analysis and high-resolution TEM-EDS mapping. Schematic of hexagonal crystal structure of  $\beta$ -TCP with details of A and B columns. Experimental HAADF-STEM images of 0.29Ag $\beta$ -TCP and pure  $\beta$ -TCP at [001] and [010] axes. See DOI: 10.1039/d0nr04208k



incorporation of atoms in  $\beta$ -TCP and characterize the naturally- and/or pathologically-incorporated elements in CaPs, it is necessary to perform detailed structural characterization of such CaPs.

Previously, ion incorporations in CaP structures have been investigated with the help of X-ray diffraction (XRD) and neutron diffraction refined by the Rietveld method, Raman spectroscopy, *ab initio* calculations, nuclear magnetic resonance, and first-principle calculations.<sup>26–33</sup> Yoshida *et al.* estimated the monovalent incorporation in either Ca(4) or Ca(5) sites of  $\beta$ -TCP with the help of lattice parameter calculations.<sup>14</sup> Matsumoto *et al.* claimed that the amount of Ag incorporation is limited to 9.09 at% with possible incorporation in Ca(4) sites and vacancies, whereas, smaller Zn ions may be incorporated in half of the Ca(5) sites simultaneously.<sup>20</sup> However, comprehensive studies have not been performed to reveal the structure of an Ag-incorporated  $\beta$ -TCP structure.

High-resolution transmission electron microscopy (HRTEM) is a powerful tool to directly observe individual incorporation at the atomic scale. However, conventional HRTEM can easily damage the  $\beta$ -TCP structure because of the beam-sensitive nature of the structure.<sup>34</sup> In this study, the estimated locations of Ag incorporation were assessed by Rietveld refinements and proven using aberration-corrected high-angle annular dark-field (HAADF)-STEM (Cs-corrected HAADF-STEM). Cs-corrected STEM has an advantage over the traditional TEM because of its lesser image degradation.<sup>35</sup> Two common approaches for reducing the damage caused by electron dosage in STEM are decreasing the pixel dwell time and lowering the beam current density, which are parameters that can be adjusted.<sup>36</sup> Cs-corrected STEM is capable of rapid scanning while avoiding possible damage during observation and simultaneously generating sub-angstrom resolution.<sup>37</sup> It has been reported that the HAADF-STEM signal is proportional to the square of the atomic number of the element, which allows an atom-by-atom chemical identification,<sup>38</sup> such as of the Ag atom in the  $\beta$ -TCP structure, the atomic number of Ag being higher than those of Ca and P atoms. This study focuses on using low-dose STEM image recording with the wide-angle data collection of the annular dark-field detector, which is advantageous for achieving a high signal/noise ratio of measurement to reach high resolution capability of the instrument.<sup>39</sup> With the help of the state-of-art HAADF-STEM observations and corresponding image simulations, we have provided an atomic insight into the location of Ag in the  $\beta$ -TCP structure, which is stabilized by incorporation of Ag atoms at specific Ca sites. To the authors' best knowledge, the present study is the first evidence of ionic incorporation in  $\beta$ -TCP performed with the state-of-art HAADF-STEM.

In the previous studies, we had clarified that the incorporation of Ag atoms stabilized the structure with a decrease in the lattice parameters, resulting in a suppression of  $\beta$ -to- $\alpha$  transformation of TCP, an improvement in thermal stability, and a decrease in bioresorbability while also exhibiting effective antibacterial activity.<sup>3,40</sup> The alteration in the properties of  $\beta$ -TCP highlights the importance of the limit of Ag

incorporation at the various sites of the  $\beta$ -TCP structure. Further, Ag incorporation can also affect the bonding of CaP coatings on metal implant materials because of increased charge transfer between the coating and metal implant.<sup>41</sup> Therefore, the properties of CaP coatings altered with ion incorporation<sup>42–44</sup> may be correlated to the findings of this study. The present study, for the first time, investigates the incorporation of Ag in Ca(4) and Ca(5) site positions of the  $\beta$ -TCP structure and estimates a possible Ag incorporation limit with the help of an atom-by-atom structural evaluation by using the state-of-art HAADF-STEM observations and corresponding simulations.

## 2. Results

The Ag-incorporated  $\beta$ -TCP with an Ag/(Ca + Ag) atomic ratio of 0.091 (0.09Ag $\beta$ -TCP), which is considered to be the theoretical limit of monovalent incorporation for Ca(4) sites,<sup>20</sup> was used to locate the Ag atoms in the Ca(4) sites of  $\beta$ -TCP. The Ag-incorporated  $\beta$ -TCP with an Ag/(Ca + Ag) atomic ratio of 0.291 (0.29Ag $\beta$ -TCP), which exceeds the theoretical limit, was investigated to access the experimental limit of Ag incorporation in  $\beta$ -TCP structure.

### 2.1. Distribution of Ag atoms in $\beta$ -TCP structure

EELS scanning (50  $\times$  50 nm) was used to observe the distribution of Ag atoms in the  $\beta$ -TCP structure, as shown in Fig. 1. The signals related to Ca, P, and O were detected homogeneously, indicating the presence of regular atoms in the  $\beta$ -TCP structure. Further, the Ag signal was well resolved and uniformly dispersed in the  $\beta$ -TCP matrix with no clustering and agreed with the TEM-EDS line analysis (ESI Fig. S2†). Even though the Ag incorporation was proven, information about the positions of the Ag atoms in the  $\beta$ -TCP structure was lacking. To confirm the position of the localized Ag atoms in the  $\beta$ -TCP structure, high-resolution TEM-EDS was conducted at a resolution of 10  $\times$  10 nm (ESI Fig. S3†). Ca and P atoms were homogeneously detected as the primary structural atoms of  $\beta$ -TCP, while some localized Ag signals could be observed from the high-resolution TEM-EDS results. However, this information was insufficient to discuss specific site incorporation. The chemical composition of the matrix of 0.29Ag $\beta$ -TCP measured by TEM-EDS is shown in Table 1. Ag concentration was 4.92 at% and the Ag/(Ca + Ag) atomic ratio was 0.12. Thus, the incorporated Ag resulted in the atomic ratio Ag/(Ca + Ag) of 0.12, thereby proving the effectiveness of the solid-state reaction method. Meanwhile, the precipitation method exhibited a maximum Ag incorporation, resulting in an atomic ratio of 0.0536 due to the formation of Ag<sub>3</sub>PO<sub>4</sub> which acts as a limiting factor.<sup>40</sup>

### 2.2. Structural model of Ag incorporation in $\beta$ -TCP

The crystal structure model of the Ag-incorporated  $\beta$ -TCP is presented in Fig. 2(a); the Ca(4) sites and vacancies are occupied by Ag atoms, shown as red spheres with half occupancy.



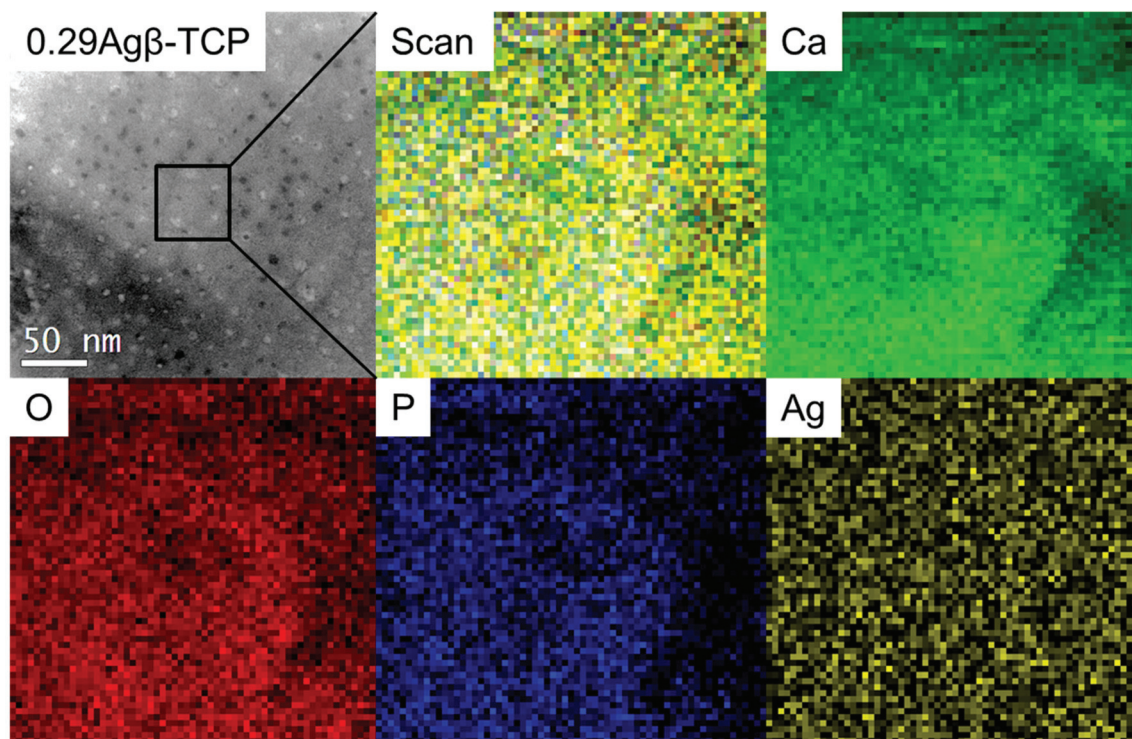


Fig. 1 STEM-EELS maps of Ca, P, and O as structural elements and Ag incorporated in 0.29Ag $\beta$ -TCP.

**Table 1** Chemical composition of O, P, Ca, and Ag in the  $\beta$ -TCP matrix of 0.29Ag $\beta$ -TCP measured by TEM-EDS

	O	P	Ca	Ag	Ag/(Ca + Ag) atomic ratio
At%	35.69 $\pm$ 3.43	22.30 $\pm$ 1.05	37.10 $\pm$ 2.32	4.92 $\pm$ 0.11	0.12

The crystal structure of  $\beta$ -TCP can be described by A and B columns along the *c*-axis (ESI Fig. S1†). The crystal structure of Ag-incorporated  $\beta$ -TCP along the [001] and [010] directions is presented in Fig. 2(b) and (c), respectively, to display the two columns. Column A, containing Ca(4) site and Ca(5) site atoms, has a unique atomic arrangement. Ca(4) sites have a large isotropic thermal parameter and long Ca–O distances. The occupancy factor of Ca(4) sites is 0.50 with Ca(4) vacancy and an atomic ratio of 4.55 mol%,<sup>10,45</sup> as presented in column A.

### 2.3. Rietveld refinement of Ag incorporation in $\beta$ -TCP

To further investigate the Ag incorporation in  $\beta$ -TCP structure, an XRD pattern of pure  $\beta$ -TCP after sintering at 1273 K was obtained, and Rietveld analysis was performed on this pattern (Fig. 3(a)). The structural parameters obtained were in good agreement with the calculated patterns. The  $\beta$ -TCP structural parameters reported in the literature<sup>10</sup> were used as the initial parameters in the Rietveld analysis. The refined structural and profile parameters of pure  $\beta$ -TCP were employed for the Rietveld analysis of the Ag-incorporated  $\beta$ -TCP structure. The

effect of Ag atom incorporation on the  $\beta$ -TCP structure was investigated for 0.09Ag $\beta$ -TCP and 0.29Ag $\beta$ -TCP.

When a higher ratio of Ag (charged atomic ratio of Ag/(Ca + Ag) = 0.29) was reacted with  $\beta$ -TCP, metallic Ag and Ag<sub>3</sub>PO<sub>4</sub> secondary phases were detected, indicating that the incorporation limit of Ag atoms in the  $\beta$ -TCP structure was reached (Fig. 3(c)). The measured atomic ratio for 0.29Ag $\beta$ -TCP was Ag/(Ca + Ag) = 0.12 (Table 1), which was slightly higher than the incorporation limit to Ca(4) sites and Ca(4) vacancies. Thus, the multiple-phase Rietveld refinement analysis of 0.29Ag $\beta$ -TCP modeled the incorporation of Ag atoms to Ca(4) sites and Ca(4) vacancies, and simultaneously replaced Ca(5) sites with Ag atoms, as shown in Fig. 3(c). The refinement results indicated that Ag atoms fully replaced the Ca(4) sites and filled the Ca(4) vacancies, corresponding to the refinement of 0.09Ag $\beta$ -TCP, indicating no incorporation in Ca(5) sites (occupancy of Ag in Ca(5) site was approximately zero).

### 2.4. HAADF-STEM of the [001] zone axis of Ag incorporation in $\beta$ -TCP

The atomic-resolution HAADF-STEM was carried out for the 0.29Ag $\beta$ -TCP and pure  $\beta$ -TCP at the [001] incident beam axis corresponding to zone axis reflections of electron diffraction (ED) patterns (ESI Fig. S4†). The ED pattern corresponds to rhombohedral  $\beta$ -TCP crystals. HAADF-STEM images were processed by fast Fourier transform (FFT) using Gatan Digital Micrograph and then filtered by masking specific (001) diffraction spots to produce an inverse FFT image (IFFT).<sup>46</sup>



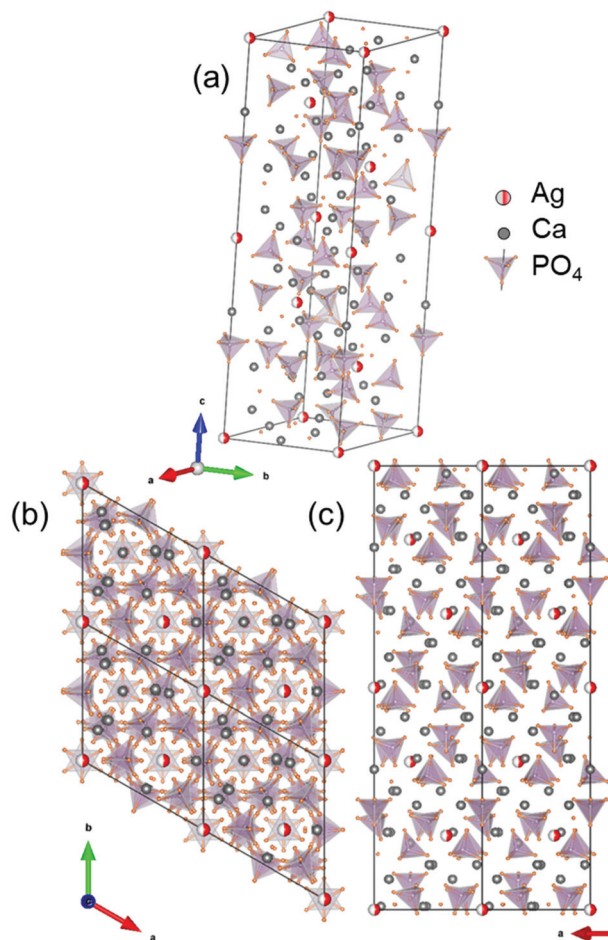


Fig. 2 Crystal structure model of (a) Ag incorporation in Ca(4) sites of  $\beta$ -TCP; the environment of Ag atoms projected along (b) [001] and (c) [010] zone axes.

IFFT HAADF-STEM image of Ag-incorporated  $\beta$ -TCP showed significant bright spots in the hexagonal order, indicated by the red spheres with half occupancy as seen in Fig. 4(a). The brightness of the HAADF-STEM image is approximately proportional to the square of the atomic number ( $Z$ ).<sup>47</sup> Thus, it is hypothesized that these hexagonal, ordered bright spots were heavier Ag atoms with an atomic number of 47 in the Ag-incorporated  $\beta$ -TCP structure existing Ca(20), P(15), O(8). Detection of a significant contrast from O atoms in the  $\beta$ -TCP structure by the HAADF-STEM technique is not expected due to their atomic number. The atomic order of Ag in the  $\beta$ -TCP structure showed considerable agreement with the atomic structure model (Fig. 4(c)), suggesting that bright Ag atoms on the A column of the  $\beta$ -TCP structure were positioned in the hexagonal structure. Meanwhile, Ca atoms on B column exhibited a blurry region between the Ag atoms located on the A column, corresponding to the Rietveld refinement as shown in Fig. 3(b and c). Although HAADF-STEM images provide useful information about the atomic order, the observations may be affected by several other factors including dynamical ED or radiation damage-induced disturbance.<sup>34,48</sup> HAADF-STEM

image simulations would help to verify the atomic ordering. Therefore, the HAADF-STEM image in the electron incidence [001] was simulated for certain Ag incorporations in the Ca(4) sites and Ca(4) vacancies of the  $\beta$ -TCP structure as shown in Fig. 4(d) with respect to the Rietveld refinement results. Simulated HAADF-STEM image of Ag-incorporated  $\beta$ -TCP appeared to be a good match to the experimental reference image (Fig. 4(a)) in terms of the location of Ag atoms as bright spots. This result was further confirmed with the intensity of the  $z$ -contrast profile from the line drawn in Fig. 4(a), exhibiting higher and lower  $z$ -values as shown in Fig. 4(e), and indicating the atoms with a higher atomic number (Ag) in A column and lower atomic number (Ca) in B column. In contrast, the P atoms were equally located in both columns. To our best knowledge, this is the first time in literature that the state-of-the-art aberration-corrected HAADF-STEM observations and corresponding multislice simulations were carried out to detect the location of incorporated atoms in CaPs, which is challenging owing to its complex and radiation-sensitive structure.

IFFT HAADF-STEM of pure  $\beta$ -TCP at the [001] incident beam axis was evaluated for comparison with the Ag-incorporated  $\beta$ -TCP structure, as shown in Fig. 4(f). The structural model and HAADF-STEM image showed good agreement for the Ca sites, as seen from the grey spheres in Fig. 4(f). The brightness associated with the Ca atoms was exhibited largely in the number of spots, indicating that the simulated HAADF-STEM image of pure  $\beta$ -TCP at the [001] incident beam axis conformed to these findings. The intensity of the  $z$ -contrast profile from the line drawn in Fig. 4(f) exhibited higher and lower  $z$ -values as shown in Fig. 4(j), suggesting that the high-density positions of Ca atoms increased the contrast. The comparison of Ag-incorporated  $\beta$ -TCP and pure  $\beta$ -TCP showed a significant intensity difference related to the Ag incorporation in the  $\beta$ -TCP structure.

## 2.5. HAADF-STEM of the [010] zone axis of Ag incorporation in $\beta$ -TCP

HAADF-STEM observation for the [010] zone axis of 0.29Ag $\beta$ -TCP and pure  $\beta$ -TCP structure (ESI Fig. S5†), which is along the  $c$ -axis, was carried out to confirm the atomic position of the excess amount of Ag atoms, which was more than the theoretical limit of the Ca(4) sites. Fig. 5(a) shows the IFFT HAADF-STEM image of the [010] zone axis confirmed with ED (Fig. 5(b)) that significantly resolved the arrangement of Ag atoms in the A columns of the  $\beta$ -TCP structure, and is illustrated in the structural model (Fig. 5(c)). The incorporated Ag atoms, observed as bright spots on the IFFT HAADF-STEM image of the [010] zone axis, were aligned nearly parallel, corresponding to the structure model where only Ca(4) sites were filled with Ag atoms. A slight distortion of the alignment of Ag atoms in the [010] zone axis as well as the [001] zone axis was due to the specimen shifting because of the poor conductivity of  $\beta$ -TCP during the scanning.

The HAADF-STEM image of the Ag-incorporated  $\beta$ -TCP structure was simulated at the [010] zone axis with Ag atoms



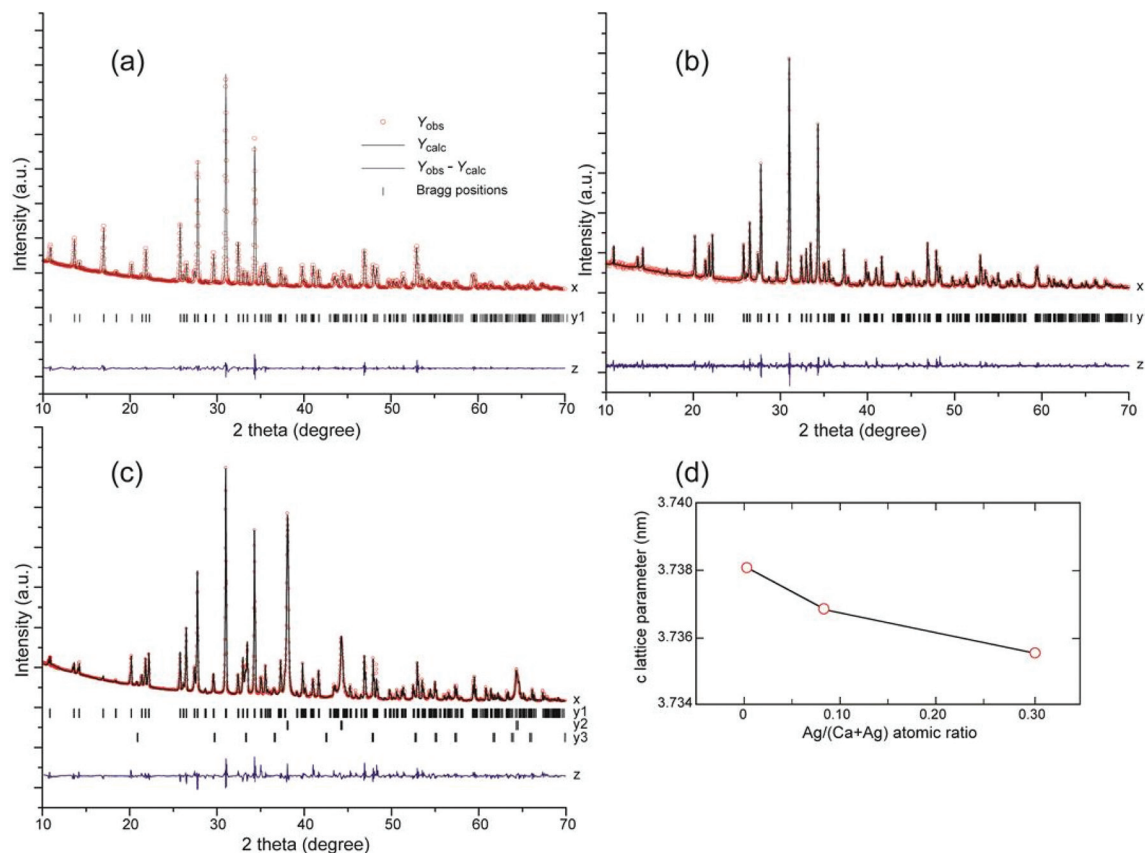


**Fig. 3** Rietveld refinement of (a) pure  $\beta$ -TCP, (b) 0.09Ag $\beta$ -TCP, and (c) 0.29Ag $\beta$ -TCP; experimental (x; red circles,  $Y_{obs}$ ) and calculated (black lines,  $Y_{calc}$ ), Bragg peak positions for (y1)  $\beta$ -TCP, (y2) metallic Ag, and (y3)  $Ag_3PO_4$ , and (z) difference curves ( $Y_{obs} - Y_{calc}$ ). (d) Variation in c lattice parameter with increase in the amount of Ag in the solid-state reaction.

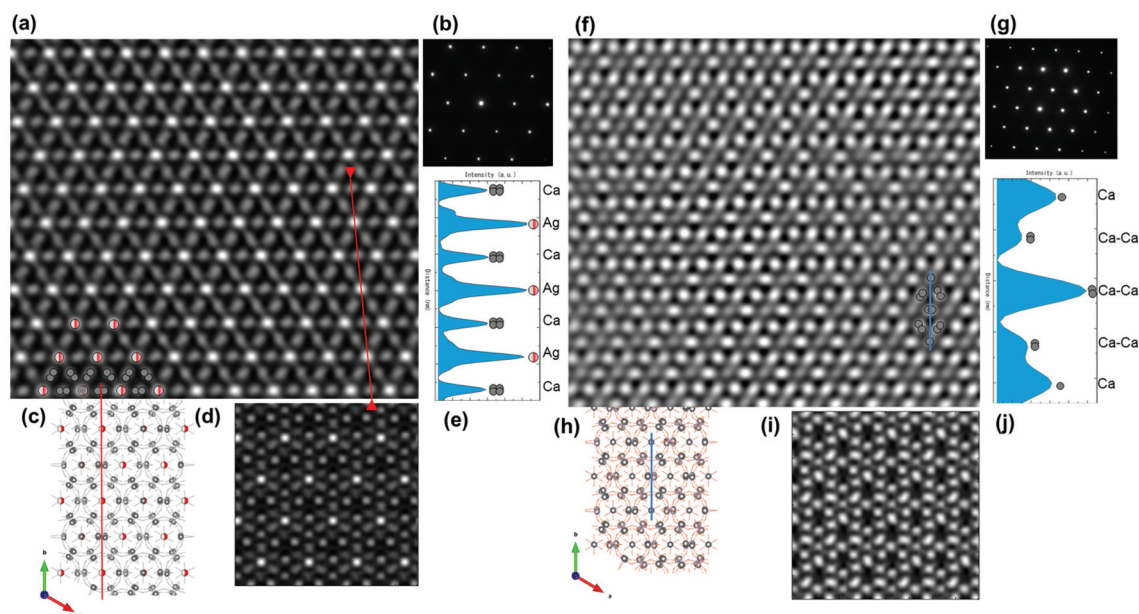


**Fig. 4** (a, f) Experimental IFFT HAADF-STEM image of the [001] zone axis of (a–e) 0.29Ag $\beta$ -TCP and (f–j) pure  $\beta$ -TCP, (b, g) diffraction pattern of the [001] zone axis, (c, h) structural model, (d, i) simulated HAADF-STEM, and (e, j) z-contrast analysis along the vertical direction of the corresponding line in the image.



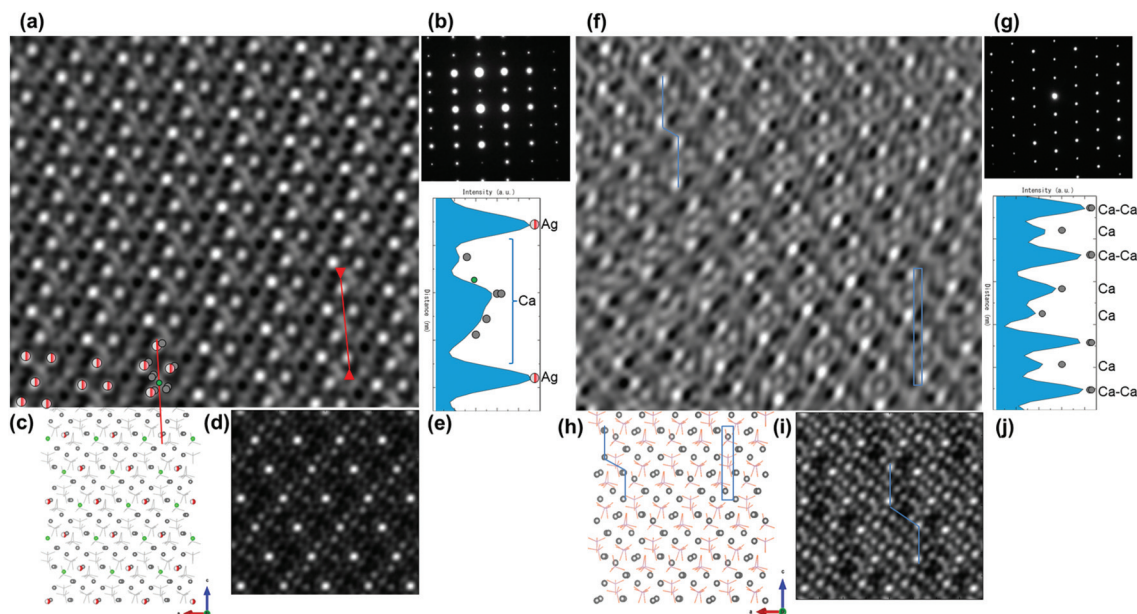


**Fig. 5** (a, f) Experimental IFFT HAADF-STEM image of the [010] zone axis of (a–e) 0.29Ag $\beta$ -TCP and (f–j) pure  $\beta$ -TCP, (b, g) diffraction pattern of the [010] zone axis, (c, h) structural model, (d, i) simulated HAADF-STEM, and (e, j) z-contrast analysis along the vertical direction of the corresponding line in the image.

incorporated in only Ca(4) sites and vacancies (Fig. 5(d)), as suggested by the Rietveld refinement. The simulated image recorded along the [010] zone axis was in good agreement with the high-intensity z-contrast spots of IFFT HAADF-STEM image at the [010] zone axis, generated by the heavy Ag atoms in the structure. The atomic projection of the proposed model with Ca(5) sites, indicated as green spheres (Fig. 5(c)), was considered to investigate the possibility of the incorporation of an excess amount of Ag atoms in Ca(5) sites. The simulated image with incorporation to only the Ca(4) site matched well with the observed HAADF-STEM image as well as the Rietveld refinement results. However, the excess amount of Ag atoms may not have been systematically incorporated in the Ca(5) sites. The intensity of the z-contrast line analysis, as depicted in Fig. 5(a), showed a significantly high value for the Ag atoms located at Ca(4) sites, whereas, widely spread signals generated by the Ca atoms, including the Ca(5) site, caused associated intensity comparable to the ratio of atomic numbers of Ag (47) and Ca (20), as shown in Fig. 5(e). The consistency between the experimental and simulated results played an important role in understanding the positioning of Ag atoms in the  $\beta$ -TCP crystal, which provided the limit of Ag incorporation.

The complexity of Ca atomic locations in  $\beta$ -TCP at [010] incident beam axis was exhibited in the Ag-incorporated  $\beta$ -TCP structure (Fig. 5(a–e)). Despite the large number of Ca locations at [010] incident beam axis, the IFFT HAADF-STEM image of pure  $\beta$ -TCP (Fig. 5(f)) was compared with the structural model and the simulated image (Fig. 5(h and i)) for the atomic locations of Ca sites, which are indicated by bright spots shown connected by lines in Fig. 5(f, h and i). The z-contrast profile (Fig. 5(j)) exhibits Ca atoms with higher intensity

due to the high-density Ca atomic locations, shown within rectangles in Fig. 5(f and h).

### 3. Discussion

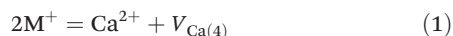
In this study, the Ag-incorporated  $\beta$ -TCP structure prepared by a solid-state reaction method led to the incorporation of Ag in the Ca(4) site of the  $\beta$ -TCP structure, exceeding the theoretical capacity of the incorporation. This result highlighted the importance of investigating the exact position and position-induced incorporation limit of Ag atoms, which can be related to other ionic incorporations. The incorporation into the CaP structure is generally preferred for improving its structural, chemical, and physical properties. However, to understand the crystallographic effect of the atomic incorporation related to the chemical and physical properties, a careful examination of structural features involved by atomic incorporation in CaPs is needed. Therefore, we proposed, for the first time, the use of state-of-the-art HAADF-STEM to analyze an Ag-incorporated  $\beta$ -TCP structure and its atom-by-atom structure basis the difference in atomic number, for determining the chemical identity of the structure at the atomic scale, precisely as envisaged by Feynman.<sup>49</sup>

No significant studies focusing on the structure of Ag-incorporated  $\beta$ -TCP have been reported. Among the few investigations that have been reported, the most relevant study is by Matsumoto *et al.*,<sup>20</sup> who reported that the maximum incorporation of monovalent metal ions for  $\beta$ -TCP was an Ag/(Ca + Ag) atomic ratio of 0.909 for Ca(4) site, including vacancies.<sup>20</sup> However, in the present study, the Ag incorporation was



measured to have reached its limit at an Ag/(Ca + Ag) atomic ratio of 0.12 in the  $\beta$ -TCP matrix of 0.29Ag $\beta$ -TCP in this study (Table 1), whereas the excess amount of Ag transformed to metallic Ag and Ag<sub>3</sub>PO<sub>4</sub> secondary phases. Based on exceeding the theoretical limit of Ca(4) site incorporation, possible incorporation in the Ca(5) site was estimated for monovalent metal ions by Yoshida *et al.*<sup>14</sup> The Rietveld refinement showed structural compliance with Ag incorporation in Ca(4) sites and vacancies, whereas the refinement results contradicted the possibility of Ca(5) site incorporation of Ag atoms (Fig. 3). The HAADF-STEM observations confirmed the Rietveld refinement results, in which no systematic Ag incorporation in Ca(5) site was detected, and there was a good agreement between HAADF-STEM images and simulations that the Ag atoms solely replaced the Ca(4) sites (Fig. 4). As Kannan *et al.* reported, Ca(5) site has a short Ca–O bond and is more favorable for the incorporation of smaller Mg or Fe (smaller than Ca) atoms rather than larger atoms (Sr),<sup>50</sup> thus supporting the findings of this study.

Furthermore, given the higher ionic radii of Ag<sup>+</sup> (0.128 nm for a six-fold coordination) compared to those of Ca<sup>2+</sup> (0.099 nm for a six-fold coordination),<sup>18</sup> Ag incorporation in the Ca site may increase the unit cell parameters. However, Ag<sup>+</sup> ions can replace Ca<sup>2+</sup> ions at Ca(4) sites and vacancies in the  $\beta$ -TCP structure while maintaining the charge balance and exchanging one Ca<sup>2+</sup> ion with two monovalent metal ions as shown in eqn (1),<sup>14</sup> forming additional oxygen bonds in the lattice.



where  $V_{Ca(4)}$  is the vacancy of Ca(4) site. Therefore, all Ca(4) sites including vacancies in the  $\beta$ -TCP structure could be occupied by the Ag<sup>+</sup> ions, resulting in a decrease in the lattice parameter  $c$  (Fig. 3(d)) and stabilization of the  $\beta$ -TCP structure. The structural stabilization due to the Ag incorporation has been reported to improve thermal stability and delay dissolution of the  $\beta$ -TCP.<sup>3,51</sup> However, there is no structural confirmation of this incorporation or microscopic evidence regarding its location in the  $\beta$ -TCP structure. Hence, it is scientifically important to confirm the location of incorporation in the  $\beta$ -TCP structure for relating the structural limit of incorporation and its effect on the properties of the  $\beta$ -TCP structure.<sup>52</sup> This confirmation is the novelty of this study.

To determine the location of excess Ag after incorporation in the Ca(4) sites, approximately 15% of the Ca(5) sites were investigated at the more complex [010] zone axis (Fig. 5). The results suggested that Ag atoms were not systematically incorporated in the Ca(5) sites. In this study, Ag atoms exceeding the theoretical limit of Ca(4) site incorporation were assumed to be irregularly located at Ca(5) sites and/or possible P sites, which can be replaced by various atoms.<sup>7</sup> The combination of the HAADF-STEM observations and simulations using the difference in  $z$ -contrast of Ag and Ca atoms proved the existence of Ag atoms located at Ca(4) sites and vacancies. The high-quality results of the HAADF-STEM imaging supported by

the results of the simulations demonstrated the direct imaging of the complex beam-sensitive  $\beta$ -TCP structures. However, the observation of the excess amount of Ag atoms in the  $\beta$ -TCP structure requires further study. The current study demonstrates that the use of HAADF-STEM can pave the way for further studies to examine various ionic incorporations in other CaP structures.

## 4. Conclusion

In this study, the crystallographic investigation of Ag incorporation in  $\beta$ -TCP structure with Rietveld analysis and the state-of-art HAADF-STEM has revealed new pertinent information on the structural location of Ag atoms in the  $\beta$ -TCP crystals. The chemical identification has proved the existence of Ag in the  $\beta$ -TCP structure to be at an individual atomic level, rather than as a cluster. Rietveld refinement of XRD patterns suggested that the Ag atoms were located in the Ca(4) sites and vacancies, whereas the incorporation in the Ca(4) vacancies balanced the valency of the crystal structure, in which the divalent Ca atoms were exchanged with the monovalent Ag atoms. This phenomenon was investigated with the help of HAADF-STEM observations at the [001] and [010] zone axes. Because of the  $z$ -contrast difference between the Ca and Ag atoms due to their atomic number, HAADF-STEM images showed significant bright spots at the location of Ag atoms. The HAADF-STEM observations at both the [001] and the [010] zone axes proved that Ag atoms were located in the low-density A columns (*i.e.*, Ca(4) and Ca(5) crystallographic sites) of the  $\beta$ -TCP crystals, although they were only incorporated in Ca(4) sites and vacancies. However, the measured Ag atoms in the  $\beta$ -TCP structure (Ag/(Ca + Ag) = 0.12) were estimated to be located in the Ca(4) sites up to an Ag/(Ca + Ag) atomic ratio of 0.0909, and the excess amount of Ag was assumed to be located randomly in the  $\beta$ -TCP structure at possible Ca(5) sites and/or P sites. The present investigation provides the first microscopic observation of incorporated atoms in a  $\beta$ -TCP structure regardless of its beam-sensitive nature and complex structure. This study established the possibility of atomic-scale observation of incorporation phenomena for various apatites.

## 5. Experimental methods

### 5.1. Specimen preparation

Pure  $\beta$ -TCP and Ag-incorporated  $\beta$ -TCP were prepared by carrying out a conventional solid-state reaction that allows a higher ratio of Ag to be incorporated, as compared with that allowed by the wet chemical process.<sup>40</sup> Ca<sub>2</sub>P<sub>2</sub>O<sub>7</sub> (Kishida Chemical Co. Ltd Osaka, Japan), CaCO<sub>3</sub> (Kishida Chemical Co. Ltd Osaka, Japan), and metallic Ag ( $\phi$  = 1  $\mu$ m, Kishida Chemical Co. Ltd Osaka, Japan) were used as the raw materials. Metallic Ag was added to prepare the Ag-incorporated  $\beta$ -TCP. The powder mix was prepared to an Ag/(Ca + Ag) atomic ratio of 0.091, which is considered to be the theoretical limit of monovalent incorpor-



ation<sup>20</sup> and an Ag/(Ca + Ag) atomic ratio of 0.291 to exceed the theoretical limit. The two cases have been hereafter referred to as 0.09Ag $\beta$ -TCP and 0.29Ag $\beta$ -TCP, respectively. The nominal value of the (Ca + Ag)/P ratio was maintained at 1.50 (ESI Table S1†). The powder mixture was processed *via* ball milling and 0.5 g of the powder was cold-pressed to pellets (10 mm in diameter and 3 mm in thickness) under a pressure of 200 MPa and sintered at 1273 K for 86.4 ks in air at heating and cooling rates of 0.05 K s<sup>-1</sup>.

### 5.2. XRD analysis

The phases and lattice parameters of sintered compacts were determined using XRD (Ultima IV, Rigaku Corp., Tokyo, Japan) with Cu K $\alpha$  radiation ( $\lambda = 1.54184$  Å). Phase analysis and Rietveld refinement were performed with X'Pert HighScore and FullProf, respectively, on XRD patterns of the Ag-incorporated  $\beta$ -TCP structure, comparing with the standard  $\beta$ -TCP structure (JCPDS#9-169). Data used for structural investigation were collected in the  $2\theta$  range 10°–70° with a 0.02° step and a counting time of 200 s per step. Commercial SiO<sub>2</sub> powders were analyzed to extract the instrumental resolution function for improving the profile fitting of the Ag-incorporated  $\beta$ -TCP structure. The sintered compacts were ground using a mortar for 3.6 ks; the obtained powder along with SiO<sub>2</sub> powder was subjected to XRD analysis. The initial structural parameters of  $\beta$ -TCP were taken from Yashima *et al.*:<sup>10</sup> space group  $R3c$ ,  $a = 10.4352$  Å and  $c = 37.4029$  Å; 18 independent atomic positions: five Ca positions (three in site 18b and two in site 6a), three P positions (two in site 18b and one in site 6a), and ten O positions. Ag<sub>3</sub>PO<sub>4</sub> and metallic Ag phases were considered to be secondary phases.

First, the Rietveld refinement was conducted with background, scale factor, zero shift, line profile parameters, lattice parameters, preferential orientations, and asymmetry parameter refinements. Then, atomic coordinates, atomic displacement factors, and site occupancies were individually and systematically checked. A statistical concept of agreement of refinement is described by  $X^2$ . Agreement factor ( $X^2$ ) can be determined from the expected and weighted profile R factors  $X^2 = (R_{wp}/R_{exp})^2$ . When a statistical agreement is reached for the observed ( $y_{obs}$ ) and calculated ( $y_{calc}$ ) structural data,  $X^2 = 1$  in the statistical limit.<sup>47</sup>

### 5.3. Microstructural observations

The model of the crystal structure of the unit cell and perspective views were visualized with VESTA, in which Ag atoms at Ca(4) sites are presented as red spheres with half occupancy in the structure model (Fig. 2). Diffraction patterns were illustrated by Recipro software at the incident beam directions parallel to the [001] and [010] of the Ag-incorporated  $\beta$ -TCP structure to confirm the experimental observations.

### 5.4. Atomic-scale evaluation using HAADF-STEM

Gatan PIPS ion milling and plasma cleaning (SOLARUS Gatan) were used for the thinning and cleaning of sintered compacts, respectively. Ion milling was conducted with a low energy elec-

tron beam at an angle of 4° to produce an electron-transparent TEM specimen. HAADF-STEM observations were carried out on JEM-ARM200F, which is fitted with Cs aberration correctors operated at 200 kV. To minimize radiation damage, STEM was operated at a low-dose condition with probe size of  $\sim 0.8$  Å and a beam current of  $\sim 10$  pA, resulting in a dose current of 0.066 pA cm<sup>-2</sup>. In contrast, the TEM mode is operated at a dose current of 68.5 pA cm<sup>-2</sup>. The chemical distribution of the incorporation of Ag was examined using electron energy-loss spectroscopy (EELS) with a 0.2 nm electron beam diameter JEM-ARM200F, equipped with energy-dispersive X-ray spectroscopy (EDS).<sup>53</sup> The images were captured by an annular dark-field detector with a collection angle from 68 to 280 mrad. The probe convergence angle was 24.45 mrad. Inverse fast Fourier transform (IFFT) HAADF-STEM images were obtained with the Gatan Digital Micrograph program.

### 5.5. Computational modeling

HAADF-STEM simulations at the [001] and [010] zone axes for the Ag-incorporated  $\beta$ -TCP structure were performed using QSTEM software.<sup>54</sup> The HAADF-STEM image simulations of Ag incorporated in the Ca(4) site of  $\beta$ -TCP structure and standard  $\beta$ -TCP structure (JCPDS#9-169) were carried out with multislice method (slice thickness, 0.5 Å) based on the structure information derived from Rietveld refinements. The following parameters were used: acceleration voltage of 200 kV, just focus (Scherzer), objective aperture angle of 25 mrad, and HAADF detector range of 70–200 mrad for the image simulations.

## Conflicts of interest

There are no conflicts to declare.

## Acknowledgements

The authors thank Dr Kobayashi of Tohoku University for his support on the TEM analyses. This study was financially supported by a Grant-in-Aid for Scientific Research from the Ministry of Education, Culture, Sports, Science and Technology (MEXT), Japan, under Contact Nos 18H01718, 18H05254, and 20H02448.

## References

- 1 L. L. Hench, *J. Am. Ceram. Soc.*, 1991, **74**, 1487–1510.
- 2 L. L. Hench, *J. Am. Ceram. Soc.*, 1998, **81**, 1705–1728.
- 3 O. Gokcekaya, K. Ueda, K. Ogasawara, H. Kanetaka and T. Narushima, *Mater. Sci. Eng., C*, 2017, **75**, 926–933.
- 4 M. Frasnelli and V. M. Sglavo, *Acta Biomater.*, 2016, **33**, 283–289.
- 5 M. Šupová, *Ceram. Int.*, 2015, **41**, 9203–9231.
- 6 J. H. Shepherd, D. V. Shepherd and S. M. Best, *J. Mater. Sci. Mater. Med.*, 2012, **23**, 2335–2347.



- 7 E. Boanini, M. Gazzano and A. Bigi, *Acta Biomater.*, 2010, **6**, 1882–1894.
- 8 J. C. Elliott, *Structure and Chemistry of the Apatites and Other Calcium Orthophosphates*, Elsevier Science, 2013.
- 9 R. Z. LeGeros, *Clin. Mater.*, 1993, **14**, 65–88.
- 10 M. Yashima, A. Sakai, T. Kamiyama and A. Hoshikawa, *J. Solid State Chem.*, 2003, **175**, 272–277.
- 11 M. Zhang, C. Wu, H. Li, J. Yuen, J. Chang and Y. Xiao, *J. Mater. Chem.*, 2012, **22**, 21686–21694.
- 12 X. Li, A. Ito, Y. Sogo, X. Wang and R. Z. LeGeros, *Acta Biomater.*, 2009, **5**, 508–517.
- 13 I. Mayer, F. J. G. Cuisinier, S. Gdalya and I. Popov, *J. Inorg. Biochem.*, 2008, **102**, 311–317.
- 14 K. Yoshida, H. Hyuga, N. Kondo, H. Kita, M. Sasaki, M. Mitamura, K. Hashimoto and Y. Toda, *J. Am. Ceram. Soc.*, 2006, **89**, 688–690.
- 15 E. Boanini, M. Gazzano, C. Nervi, M. R. Chierotti, K. Rubini, R. Gobetto and A. Bigi, *J. Funct. Biomater.*, 2019, **10**, 20.
- 16 A. Jacobs, M. Gaulier, A. Duval and G. Renaudin, *Crystals*, 2019, **9**(7), 326.
- 17 S. Hoover, S. Tarafder, A. Bandyopadhyay and S. Bose, *Mater. Sci. Eng., C*, 2017, **79**, 763–769.
- 18 P. N. Lim, L. Chang and E. S. Thian, *Nanomedicine*, 2015, **11**, 1331–1344.
- 19 U. S. Hashimoto, K. Yoshida, Y. Toda and T. Kanazawa, *Phosphorus Res. Bull.*, 2002, **13**, 123–126.
- 20 N. Matsumoto, K. Sato, K. Yoshida, K. Hashimoto and Y. Toda, *Acta Biomater.*, 2009, **5**, 3157–3164.
- 21 S. Liu, C. Fan, F. Jin, L. Zhao, K. Dai and J. Lu, *Int. J. Appl. Ceram. Technol.*, 2015, **12**, 294–299.
- 22 C. Piccirillo, R. C. Pullar, D. M. Tobaldi, P. M. Lima Castro and M. M. Estevez Pintado, *Ceram. Int.*, 2015, **41**, 10152–10159.
- 23 A. Ewald, D. Hösel, S. Patel, L. M. Grover, J. E. Barralet and U. Gbureck, *Acta Biomater.*, 2011, **7**, 4064–4070.
- 24 T. N. Kim, Q. L. Feng, J. O. Kim, J. Wu, H. Wang, G. C. Chen and F. Z. Cui, *J. Mater. Sci. Mater. Med.*, 1998, **9**, 129–134.
- 25 M. Raza, S. Zahid and A. Asif, in *Woodhead Publishing Series in Biomaterials*, ed. A. S. Khan and A. A. Chaudhry, Woodhead Publishing, 2020, pp. 21–51.
- 26 X. Wei and M. Akinc, *J. Am. Ceram. Soc.*, 2007, **90**, 2709–2715.
- 27 M. Yashima and Y. Kawaike, *Chem. Mater.*, 2007, **19**, 3973–3979.
- 28 S. Gomes, J.-M. Nedelec, E. Jallot, D. Sheptyakov and G. Renaudin, *Chem. Mater.*, 2011, **23**, 3072–3085.
- 29 S. Gomes, J.-M. Nedelec, E. Jallot, D. Sheptyakov and G. Renaudin, *Cryst. Growth Des.*, 2011, **11**, 4017–4026.
- 30 S. Kannan, F. Goetz-Neunhoffer, J. Neubauer and J. M. F. Ferreira, *J. Am. Ceram. Soc.*, 2008, **91**, 1–12.
- 31 L. Obadia, P. Deniard, B. Alonso, T. Rouillon, S. Jobic, J. Guicheux, M. Julien, D. Massiot, B. Bujoli and J.-M. Bouler, *Chem. Mater.*, 2006, **18**, 1425–1433.
- 32 F. Ren, Y. Leng, R. Xin and X. Ge, *Acta Biomater.*, 2010, **6**, 2787–2796.
- 33 K. Matsunaga, T. Kubota, K. Toyoura and A. Nakamura, *Acta Biomater.*, 2015, **23**, 329–337.
- 34 N. Rangavittal, A. R. Landa-Cánovas, J. M. González-Calbet and M. Vallet-Regí, *J. Biomed. Mater. Res.*, 2000, **51**, 660–668.
- 35 T. J. Pennycook, G. T. Martinez, P. D. Nellist and J. C. Meyer, *Ultramicroscopy*, 2019, **196**, 131–135.
- 36 J. P. Buban, Q. Ramasse, B. Gipson, N. D. Browning and H. Stahlberg, *J. Electron Microsc.*, 2009, **59**, 103–112.
- 37 K. Sohlberg, T. J. Pennycook, W. Zhou and S. J. Pennycook, *Phys. Chem. Chem. Phys.*, 2015, **17**, 3982–4006.
- 38 O. L. Krivanek, M. F. Chisholm, V. Nicolosi, T. J. Pennycook, G. J. Corbin, N. Dellby, M. F. Murfitt, C. S. Own, Z. S. Szilagy, M. P. Oxley, S. T. Pantelides and S. J. Pennycook, *Nature*, 2010, **464**, 571–574.
- 39 K. Gnanasekaran, G. de With and H. Friedrich, *R. Soc. Open Sci.*, 2020, **5**, 171838.
- 40 O. Gokcekaya, K. Ueda, T. Narushima and C. Ergun, *Mater. Sci. Eng., C*, 2015, **53**, 111–119.
- 41 D. Arcos and M. Vallet-Regí, *J. Mater. Chem. B*, 2020, **8**, 1781–1800.
- 42 O. Gokcekaya, T. J. Webster, K. Ueda, T. Narushima and C. Ergun, *Mater. Sci. Eng., C*, 2017, **77**, 556–564.
- 43 M. Qadir, Y. Li and C. Wen, *Acta Biomater.*, 2019, **89**, 14–32.
- 44 J. Wu, K. Ueda and T. Narushima, *Mater. Sci. Eng., C*, 2020, **109**, 110599.
- 45 N. Matsumoto, K. Yoshida, K. Hashimoto and Y. Toda, *Mater. Res. Bull.*, 2009, **44**, 1889–1894.
- 46 T. Hayashi, H. Muramatsu, D. Shimamoto, K. Fujisawa, T. Tojo, Y. Muramoto, T. Yokomae, T. Asaoka, Y. A. Kim, M. Terrones and M. Endo, *Nanoscale*, 2012, **4**, 6419–6424.
- 47 B. H. Toby, *Powder Diff.*, 2006, **21**, 67–70.
- 48 Z. L. Wang and J. M. Cowley, *Ultramicroscopy*, 1989, **31**, 437–453.
- 49 P. N. Lim, L. Chang and E. S. Thian, *Nat. Nanotechnol.*, 2009, **4**, 781.
- 50 S. Kannan, F. Goetz-Neunhoffer, J. Neubauer, S. Pina, P. M. C. Torres and J. M. F. Ferreira, *Acta Biomater.*, 2010, **6**, 571–576.
- 51 O. Gokcekaya, K. Ueda and T. Narushima, *Ceram. Trans.*, 2015, **254**, 13–20.
- 52 M. Sayahi, J. Santos, H. El-Feki, C. Charvillat, F. Bosc, I. Karacan, B. Milthorpe and C. Drouet, *Mater. Today Chem.*, 2020, **16**, 100230.
- 53 M. Meledina, S. Turner, V. V. Galvita, H. Poelman, G. B. Marin and G. Van Tendeloo, *Nanoscale*, 2015, **7**, 3196–3204.
- 54 C. T. Koch, Ph.D. Thesis, 2002.

